Correlation of optical conductivity and pairing states in superconducting Weyl semimetals

Jun Fang,[1] Chao Zhang,[2] Haiqing Lin,[3] and Zhongshui Ma[4,*]
[1]*School of Physics, Peking University, Beijing 100871, China*
[2]*School of Physics, University of Wollongong, Wollongong, New South Wales 2522, Australia*
[3]*School of Physics, Zhejiang University, Hangzhou 310027, China*
[4]*School of Mechanical, Materials, Mechatronic and Biomedical Engineering, University of Wollongong, Wollongong, New South Wales 2522, Australia*

(Received 11 February 2024; revised 21 June 2024; accepted 9 July 2024; published 22 July 2024)

There are two different pairing potentials for the superconductivity of doped Weyl semimetals, i.e., the internode BCS pairing and the intranode Fulde-Ferrell-Larkin-Ovchinnikov (FFLO) pairing. We show that the superconducting pairing potentials can be clearly distinguished from the frequency characteristics of optical conductivity. The pairing-dependent optical conductivities for the BCS and FFLO pairings are calculated. The optical conductivities exhibit two types of distinct resonances, the Van Hove resonance for the BCS pairing and the resonance with a threshold for FFLO pairing. The result provides a method of identifying the pairing potential in superconducting Weyl semimetals.

DOI: 10.1103/PhysRevB.110.014515

I. INTRODUCTION

The superconductivity in Weyl semimetals (WSMs) has attracted a great deal of attention since the discovery of WSMs [1]. It has been predicted that the superconducting Weyl semimetals (SWSMs) exhibit unconventional superconductivity [2–6]. The energy gap created by the pairing of electrons is the most important parameter of a superconductor. Due to the presence of even pairs of Weyl nodes at the Fermi level, the nodes give rise to a rich phase space for electrons to pair so that the preferred superconducting pairings become an enigmatic concept in the SWSMs [2–9]. The first-principle calculations have shown that even pairs of Weyl nodes at the Fermi level participate in the formation of the condensate and result in a nodal superconducting phase. Correspondingly, two pairing mechanisms have been proposed theoretically for realizing the superconductivity in doped WSMs. The internode BCS pairing (the BCS pairing mechanism) is formed by two fermions from two nodes with different chiralities, while the intranode Fulde-Ferrell-Larkin-Ovchinnikov (FFLO) pairing (the FFLO pairing mechanism) [10] is formed by two fermions in the same node with the same chirality. The Cooper pair associated with BCS pairing has zero momentum. The Cooper pair formed by the FFLO pairing has a finite total momenta, and the superconducting order parameter is spatially nonuniform [11,12]. Disconnected sheets of the Fermi surface due to the nodes can result in different superconducting energy gaps. Previous studies showed that the BCS paired states are topologically nontrivial with gapless nodes in the energy dispersion and the FFLO paired state is topologically trivial with a full gap [13]. It has been shown that in WSM/SWSM hybrid structures, the transport characteristics of SWSMs are closely correlated to the microscopic origin of the pairing symmetry [14–17]. Although a variety of theoretical investigations on the properties of superconducting states in SWSMs have been carried out, definitive experimental identification of the pairing potential is still lacking.

A superconductor is usually characterized by a superconducting energy gap created by the pairing of electrons. Probing the structure of the energy gap is a central challenge for elucidating the mechanism of superconductivity. Various indirect methods have been carried out with the aim of determining the superconducting energy gap in conventional and unconventional superconductors, such as Josephson interferometry [18], optical spectroscopy [19], and Andreev-reflection spectroscopy [20].

Among these, optical detection methods have been used to obtain and identify information on the pairing symmetry and characteristics of the superconducting gap [21]. Infrared (IR) spectroscopy has been used to obtain the energy gap information [22–24]. It can reveal the dynamical properties of superconductors and the quasiparticle information that might be difficult to explore by other means. Besides the electronic structure, the optical response is directly related to the optical self-energy or memory function, which describes the function of the mass enhancement factor and unrenormalized scattering rate [25–28]. In recent years, the IR technique has been extensively used to study unconventional superconductors [29–32], high-T_c superconductors [33–35], iron-based superconductors [36–43], and topological superconductors [44]. Superconductors [32,45,46] with breaking inversion symmetry and the optical properties of the related parent materials, such as Dirac and Weyl semimetals [47–51], have been studied. IR behavior without momentum conservation [52] is described by the Mattis-Bardeen formula in the dirty limit [52–54]. This

*Contact author: zma@uow.edu.au

method has been used to study the optical response with the topological characteristic of superconducting gaps [55–57] in SWSMs.

In this work we demonstrate that the different superconducting pairings (FFLO and BCS) in SWSMs can be clearly identified in optical conductivity because the FFLO and BCS ground states are topologically different. The theoretical calculations show signatures of node point symmetries on the superconducting energy gap. Different from the isotropic characteristics of the FFLO energy gap, the BCS gap manifests anisotropy due to node-dependent pairing in Weyl superconductors. It is found that the optical response has a close correlation with the formation of BCS and FFLO pairings. Under the BCS pairing the gap function goes to zero at certain points in momentum space. On the other hand, the gap under the FFLO pair is momentum dependent. These two different gaps lead to significant differences in the optical response. We analyze the optical conductivity of SWSMs with two different pairings for the bulk (clean limit) and the surface (thin film or dirty) states. For the bulk states, the momentum is conserved in the scattering so that the optical conductivity in the clean limit can be calculated with the Kubo formula [58]. However, there is a lack of momentum conservation in the thin film or dirty SWSM. By assuming that the Mattis-Bardeen theory applies to SWSMs, infrared behaviors without momentum conservation will be analyzed using the Mattis-Bardeen formula [52–54].

We found that in the clean limit, the optical conductivity has an extra transition which is absent in normal metals. This transition is induced by the charge conjugation of quasiparticles in the conduction and valence bands. The optical conductivity is symmetrical about the charge transport direction and the light polarization direction. In the BCS case, the real and imaginary parts of the optical conductivity have the same exponential relationship to the photon energy when the photon energy is lower than the pairing potential [59]. However, in the thin film or dirty SWSM, the optical response can be described by the dirty-limit Mattis-Bardeen-type response with an isotropic gap for FFLO pairing. For the BCS pairing, the optical response is described by an angle-dependent version of the Mattis-Bardeen formula. We show that the real part of the optical conductivity of SWSMs with FFLO pairing has a threshold value for the photon energy due to the fully gapped band structure. The optical conductivity of SWSMs with BCS pairing starts from zero photon energy. The optical conductivity for dirty SWSMs can be directly probed in experiment. We find that the frequency dependence of the optical conductivity has a very close correlation with the topological band structure in SWSMs. This finding provides an experimental method to identify the pairing potential in SWSMs.

II. MODELS AND HAMILTONIAN

A WSM with broken time-reversal symmetry is described by the Hamiltonian

$$H=\sum_{\kappa}\xi^{\dagger}_{\mathbf{k}_\kappa,\kappa}h_\kappa(\mathbf{k},b)\xi_{\mathbf{k}_\kappa,\kappa}-\mu\xi^{\dagger}_{\mathbf{k}_\kappa,\kappa}\xi_{\mathbf{k}_\kappa,\kappa}+H_I, \tag{1}$$

where $h_\kappa(\mathbf{k},b)=v_F\boldsymbol{\sigma}\cdot\mathbf{k}_\kappa$ and $\mathbf{k}_\kappa=(k_x,k_y,\kappa k_z-b)$. The two Weyl nodes are located at $\mathbf{Q}_\pm=(0,0,\pm b)$ with a chirality of $\kappa=\pm$, $\boldsymbol{\sigma}$ are the Pauli matrices in the spin space, v_F is the Fermi velocity, and $\xi_{\mathbf{k}_\kappa,\kappa}=(d_{\mathbf{k}_\kappa,\kappa,\uparrow},d_{\mathbf{k}_\kappa,\kappa,\downarrow})^{\mathcal{T}}$, with $\mathcal{T}$ being a transpose operation for a Weyl spinor, in which the annihilation (creation) operator of the Weyl fermions with momentum $\mathbf{k}_\kappa=\mathbf{k}+\mathbf{Q}_\kappa$ $d_{\mathbf{k}_\kappa,\kappa,\sigma}$ ($d^{\dagger}_{\mathbf{k}_\kappa,\kappa,\sigma}$) is dependent on several quantum numbers due to their dependence on node points and spins. H_I is the electron-electron interaction. Under the assumption of an s-wave short-range pairing potential between Weyl fermions [3], H_I can be written as [13]

$$H_I=\sum_{\kappa,\kappa',\kappa'',\kappa'''}\int\frac{d\mathbf{k}d\mathbf{k}'}{(2\pi\hbar)^6}\delta_{\kappa+\kappa'-\kappa''-\kappa'''}\times V_{\kappa\kappa'}d^{\dagger}_{\mathbf{k}_\kappa,\kappa,\uparrow}d^{\dagger}_{-\mathbf{k}_{-\kappa'},\kappa',\downarrow}d_{-\mathbf{k}'_{-\kappa''},\kappa'',\downarrow}d_{\mathbf{k}'_{\kappa'''},\kappa''',\uparrow}, \tag{2}$$

where $\delta_{(\dots)}$ represents a constraint on the nodes where interacting electrons reside. An electron can interact with electrons in the same node ($\kappa=\kappa'=\kappa''=\kappa'''$; we refer to this as FFLO pairing) or with electrons from a different node ($\kappa+\kappa'=\kappa''+\kappa'''=0$) with the opposite chirality (we refer to this as BCS pairing). As a consequence, the interaction strength $V_{\kappa\kappa'}$ depends on not only the momenta of interacting fermions but also the nodes to which the interacting electrons belong. For a δ function with four variables, three would be arbitrary. However, in the present case in which each κ can take only a value of ±1, the constraint imposed by the δ function leaves only two arbitrary κ. To make a distinction between the intranode and internode interactions we denote $V_F=V_{\kappa,\kappa}$ for the intranode interaction and $V_B=V_{\kappa,-\kappa}$ the for internode interaction. Then H_I consists of H_I^F and H_I^B, where $H_I^F=(2\pi\hbar)^{-6}\sum_\kappa\int d\mathbf{k}d\mathbf{k}'V_Fc^{\dagger}_{\mathbf{k}_\kappa,\kappa,\uparrow}d^{\dagger}_{-\mathbf{k}_{-\kappa},\kappa,\downarrow}d_{-\mathbf{k}'_{-\kappa},\kappa,\downarrow}d_{\mathbf{k}'_k,\kappa,\uparrow}$, with the same momentum shift related to the node, and $H_I^B=(2\pi\hbar)^{-6}\sum_{\kappa,\kappa'}\int d\mathbf{k}d\mathbf{k}'V_Bd^{\dagger}_{\mathbf{k}_\kappa,\kappa,\uparrow}d^{\dagger}_{-\mathbf{k}_{-\kappa},-\kappa,\downarrow}d_{-\mathbf{k}\kappa'',-\kappa',\downarrow}d_{\mathbf{k}\kappa'',\kappa',\uparrow}$, with the Cooper pair having zero total momentum.

To calculate the response of light, we define the node-dependent Green's function $G_\kappa(\mathbf{k},\tau-\tau')=-\langle T_\tau d_{\mathbf{k},\kappa}(\tau)d^{\dagger}_{\mathbf{k},\kappa}(\tau')\rangle$ and the correlation functions $F_{\lambda,\kappa}(\mathbf{k},\tau-\tau')=\langle T_\tau\widetilde{d}_{-\mathbf{k},\kappa}(\tau)d^{T}_{\mathbf{k},\lambda\kappa}(\tau')\rangle$ and $F^{\dagger}_{\lambda,\kappa}(\mathbf{k},\tau-\tau')=\langle T_\tau d^{\dagger T}_{-\mathbf{k},\lambda\kappa}(\tau)\widetilde{d}^{\dagger}_{-\mathbf{k},\kappa}(\tau')\rangle$, where T_τ is the time-ordering operator in imaginary time τ, $\widetilde{d}_{k,\kappa}=(d_{k,\kappa,\downarrow},d_{k,\kappa,\uparrow})^T$, the subscript $\lambda=F$ for the intranode pairing, and $\lambda=B$ for the internode pairing. The correlation functions have the following symmetry properties: $F_{B,-\kappa,\downarrow\uparrow}(\mathbf{k},0)=-F_{B,\kappa,\uparrow\downarrow}(-\mathbf{k},0)=-F_{B,\kappa,\uparrow\downarrow}(\mathbf{k},0)$ and $F_{F,\kappa,\downarrow\uparrow}(\mathbf{k},0)=-F_{F,\kappa,\uparrow\downarrow}(-\mathbf{k},0)=-F_{F,\kappa,\uparrow\downarrow}(\mathbf{k},0)$. The gap functions for the BCS and FFLO pairings are given by $\Delta_B=-\sum_{\kappa'}(2\pi\hbar)^{-3}\int d\mathbf{k}V_BF_{B,-\kappa',\downarrow\uparrow}(\mathbf{k},0)$ and $\Delta_F=-(2\pi\hbar)^{-3}\int d\mathbf{k}V_FF_{F,\kappa,\downarrow\uparrow}(\mathbf{k},0)$, respectively.

The equations of motion for the Green's function and the correlation functions are written as

$$\delta(\tau-\tau')=[-\hbar\partial_\tau-(h_\kappa(\mathbf{k},b)-\mu)]G_{\lambda,\kappa}(\mathbf{k},\tau-\tau')+\Delta_\lambda\sigma_zF^{\dagger}_{\lambda,\kappa}(\mathbf{k},\tau'-\tau), \tag{3}$$

$$0=[-\hbar\partial_\tau-(h_\kappa(\mathbf{k},b)+\mu)]F^{\dagger}_{B,-\kappa}(\mathbf{k},\tau'-\tau)+\Delta^*_B\sigma_zG_{B,\kappa}(\mathbf{k},\tau-\tau'), \tag{4}$$

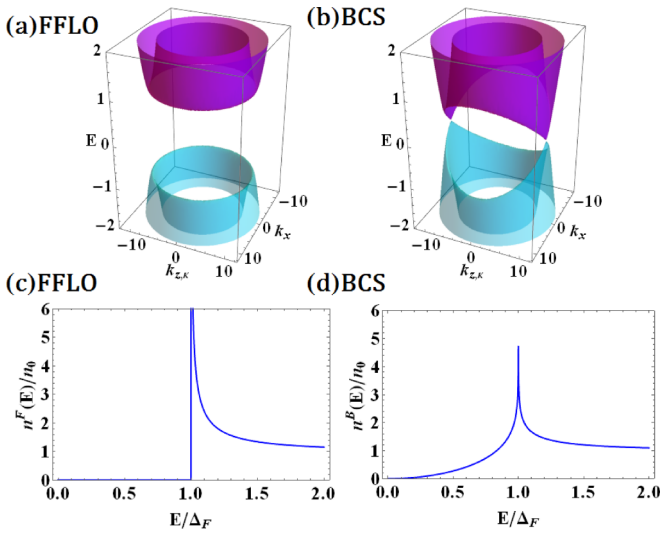

FIG. 1. Energy spectra and density of states for SWSMs with the FFLO and BCS pairings. (a) Energy spectrum for the FFLO pairing. (b) Energy spectrum for the BCS pairing. (c) The density of states for the FFLO pairing. (d) The density of state for the BCS pairing.

and

$$0 = [-\hbar\partial_\tau - (h_{-\kappa}(\mathbf{k}, -b) + \mu)]F^\dagger_{F,\kappa}(\mathbf{k}, \tau' - \tau) + \Delta_F^* \sigma_z G_{F,\kappa}(\mathbf{k}, \tau - \tau'), \tag{5}$$

with $\lambda = 1$ (-1) for the FFLO (BCS) pairing. By applying the Fourier transformation to Eqs. (3)–(5), we can obtain the Green's function and correlation functions for FFLO and BCS pairings, respectively. The energy spectra for FFLO pairing ($\Delta_B = 0$ and $\Delta_F \neq 0$) and for BCS pairing ($\Delta_B \neq 0$ and $\Delta_F = 0$) are found to be

$$E^{\eta,\gamma}_{\kappa,\zeta}(\mathbf{k}) = \begin{cases} \eta\beta\sqrt{(v_F k_\kappa - \zeta\mu)^2 + \Delta_F^2}, & \gamma: F, \\ \eta\beta\sqrt{\Delta_B^2 + v_F^2 k^2 + \mu^2 - 2\zeta v_F\sqrt{\Delta_B^2 k_z^2 + k^2\mu^2}}, & \gamma: B, \end{cases} \tag{6}$$

and the densities of states are $n^F(E) = (E/\sqrt{E^2 - \Delta_F^2})n_0$ and $n^B(E) = (E/2\Delta_B)\mathrm{Re}[\ln(E + \Delta_B)/(E - \Delta_B)]n_0$, where $\eta = +(-)$ denotes electrons (holes), $\zeta = +(-)$ denotes the conduction (valence) band, and $n_0 = \mu^2/(2\pi^2\hbar^3 v_F^3)$. Figure 1(a) shows that the spectrum for SWSMs with FFLO pairing is gapped and isotropic. Correspondingly, the density of states vanishes within the gap but diverges at the edge of the gap, as shown in Fig. 1(c). Figure 1(b) shows that the spectrum for SWSMs with BCS pairing is anisotropic and gapless at $(0, 0, \pm\sqrt{\Delta_B^2 + \mu^2})$. The density of states is nonzero except at $E = 0$ and has a sharp peak at $E = \Delta_B$, as shown in Fig. 1(d). Comparing SWSMs to a regular superconductor with FFLO pairing [60], the densities of states are qualitatively different. In SWSMs the FFLO pairing is intranode pairing from the same Weyl node. The order parameter in Ref. [60] is an oscillatory function in real space changing from zero to Δ_F. As a result, the density of states is nonzero everywhere. In the present SWSM, the order parameter is nonzero everywhere in momentum space. The gap opens uniformly, as shown in Fig. 1(a). Therefore, the quasiparticle density of states vanishes within the gap $E < \Delta_F$.

That the FFLO pairing H_I^F in SWSM is significantly different from the FFLO pairing in conventional superconductor could be due to the following effects. (1) The first is special Fermi surfaces. In the Weyl semimetal, the Fermi surface consists of two disconnected sheets around the Weyl nodes. The effective low-energy theory of a Weyl semimetal corresponds to electrons located close to Weyl nodes. The intranode pairing is created between electrons from the opposite parts of each Fermi surface sheet at individual Weyl nodes; i.e., the momentum of each Cooper pair is equal to the momentum of the Weyl node center such that the FFLO state has a center of momentum twice the position vector of the Weyl node. (2) In the linear dispersion relation, the density of states goes to zero at the Weyl point compared to a system with parabolic dispersion. As a consequence of the vanishing density of states, a minimum interaction strength is required to nucleate quasiparticles. The system is gapped as expected. (3) Another effect is the spin-momentum locking in SWSMs for pairing of opposite spin states. The differences between the FFLO states on Zeeman-split Fermi surfaces (regular superconductor) and those on SWSM with spin-momentum locking is also due to the spin texture picture. Each momentum state on the Weyl cone has a definite spin direction, a property known as spin-momentum locking. (4) When there is only intranode coupling, H_I^F does not couple different Weyl nodes.

III. OPTICAL CONDUCTIVITY

The optical conductivity is calculated by using the Kubo formula $\sigma_{\alpha\gamma}(\mathbf{q}, \Omega) = (i\Omega^{-1})K_{\alpha\gamma}(\mathbf{q}, \Omega)$. $K_{\alpha\gamma}(\mathbf{q}, i\Omega)$ is the current-current correlation function,

$$K_{\alpha\gamma}(\mathbf{q}, i\Omega) = -\frac{1}{V}\int_0^{\hbar\beta} d\tau e^{i\Omega\tau/\hbar} Tr\langle j_\alpha(\mathbf{q}, \tau) j_\gamma(-\mathbf{q}, 0)\rangle. \tag{7}$$

The current operator is given as

$$j_\alpha(\mathbf{q}, \tau) = -\frac{1}{(2\pi\hbar)^3}\sum_\kappa \int d^3\boldsymbol{k} e v_F \xi^\dagger_{\mathbf{k}+\mathbf{q},\kappa}(\tau)\sigma_{\alpha,\kappa}\xi_{\mathbf{k},\kappa}(\tau), \tag{8}$$

with $\sigma_{\alpha,\kappa} = (1 - 2\delta_{\kappa,-1}\delta_{\alpha,z})\sigma_\alpha$. V is the volume of the system, and $\beta = (k_B T)^{-1}$. $K_{\alpha\gamma}(q, i\Omega)$ can be written in the form

$$K_{\alpha\gamma}(q, i\Omega) = K^{(G)}_{\alpha\gamma}(q, i\Omega) + K^{(C)}_{\alpha\gamma}(q, i\Omega), \tag{9}$$

where $K^{(\chi)}_{\alpha\gamma}(q, i\Omega)$ with $\chi = G$ (C) is the Green's (correlation) function. We now transform these functions into the Matsubara frequency space $\omega_n = [(2n + 1)\pi/\beta]$, with $n = 0, \pm1, \pm2, \ldots$, $G_\kappa(\mathbf{k}, i\omega_n) = \int_0^{\hbar\beta} d\tau e^{i\omega_n\tau/\hbar} G_\kappa(\mathbf{k}, \tau)$, and $F_{\lambda,\kappa}(\mathbf{k}, i\omega_n) = \int_0^{\hbar\beta} d\tau e^{i\omega_n\tau/\hbar} F_{\lambda,\kappa}(\mathbf{k}, \tau)$. We obtain $K^{(\chi)}_{\alpha\gamma}(q, i\Omega) = (2\pi\hbar)^{-3}(ev_F)^2\beta^{-1}\sum_\kappa\sum_n \int d\mathbf{k} Tr\boldsymbol{\Sigma}^{(\chi)}(\mathbf{k}, \mathbf{q}, i\omega_n, \Omega)$, with

$$\boldsymbol{\Sigma}^{(G)}(\mathbf{k}, \mathbf{q}, i\omega_n, \Omega) = -[G_\kappa(\mathbf{k} + \mathbf{q}, i\omega_n + i\Omega) \times \sigma_{\alpha,\kappa} G_\kappa(\mathbf{k}, i\omega_n)\sigma_{\gamma,\kappa}] \tag{10}$$

and

$$\mathbf{\Sigma}^{(C)}(\mathbf{k},\mathbf{q},i\omega_n,\Omega)=\big[F^{\dagger,T}_{\lambda,\kappa}(-\mathbf{k}-\mathbf{q},i\omega_n+i\Omega)\times\sigma_x\sigma_{\alpha,\kappa}\sigma_x F_{\lambda,\kappa}(-\mathbf{k},i\omega_n)\sigma^*_{\gamma,\kappa}\big],\quad(11)$$

where the sum is over the Matsubara frequencies.

The optical conductivity of superconductors consists of two parts: the bulk contribution and the surface contribution. They are spatially different. We will first discuss the bulk optical conductivities for SWSMs with the FFLO and BCS pairings.

(1) *FFLO pairing.* For FFLO pairing, $\varepsilon^F_\zeta(k)=\sqrt{\Delta_F^2+(v_Fk_\kappa+\xi\mu)^2}$. For small $|\mathbf{q}|$, $|\mathbf{k}+\mathbf{q}|\approx k+\mathbf{q}\cdot\widehat{\mathbf{k}}$, and $\varepsilon^F_\zeta(k+q)\approx\varepsilon^F_\zeta(k)+\delta\varepsilon^{F,1}_\zeta+\delta\varepsilon^{F,2}_\zeta$, where $\delta\varepsilon^{F,1}_\zeta=v_F\mathbf{q}\cdot\widehat{\mathbf{k}}_\kappa(v_Fk_\kappa+\zeta\mu)/\varepsilon^F_\zeta(\mathbf{k})$, $\delta\varepsilon^{F,2}_\zeta=(v_F\mathbf{q}\cdot\widehat{\mathbf{k}}_\kappa)^2\Delta_F^2/2[\varepsilon^F_\zeta(\mathbf{k})]^3$, and $\widehat{\mathbf{k}}$ is the direction of $\mathbf{k}$. In the infrared and low-temperature regime, $\Omega\approx\Delta_{F/B}$, and $k_BT\ll\Omega\ll\mu$. For $\zeta=+$, the energy is much higher than $2\Delta_F$, so that only the $\zeta=-$ state contributes to the infrared absorption. Under these considerations, the optical conductivity is given as

$$\sigma^F_{\alpha\alpha}(q,\Omega)=\frac{i(ev_F)^2\hbar}{\Omega}\int\frac{d^3k}{(2\pi\hbar)^3}\hat{k}_\alpha^2\tanh\frac{\beta\varepsilon^F_-(\mathbf{k})}{2}\times\frac{2\Delta_F^2(v_F\mathbf{q}\cdot\hat{\mathbf{k}})^2}{\varepsilon^F_-(\mathbf{k})\Omega^3}\left(\frac{1}{\tilde{\Omega}+2\varepsilon^F_-(k)}+\frac{1}{\tilde{\Omega}-2\varepsilon^F_-(k)}\right),\quad(12)$$

where $\tilde{\Omega}=\Omega+i0$. For the conductivity of SWSMs in a clean limit described by Eq. (12), the electron-impurity scattering is absent, and the scattering time is infinitely long. In other words, the optical conductivity is not related to the drift velocity but is governed by the direct band-to-band transition.

It is found that in the lowest order, $\sigma_{\alpha\alpha}$ vanishes as q goes to zero. This behavior is different from that of normal metals because $\sigma^{F,(G)}_{\alpha\alpha}(0,\Omega)=-\sigma^{F,(C)}_{\alpha\alpha}(0,\Omega)$. From the microscopical point of view, the quasiparticles of hole and electron states with the same chirality have the opposite charges, so that a quasiparticle cannot jump to the higher energy level simply by absorbing a photon. Because optical conductivity is an odd function of k, the terms in the first order of q do not contribute to $\sigma_{\alpha\alpha}$. As a result, the leading order of the nonzero contribution to $\sigma^F_{\alpha\alpha}$ is proportional to q^2.

Because the energy spectrum is isotropic with FFLO pairing, $\sigma^F_{zz}=\sigma^F_{yy}=\sigma^F_{xx}$. As an example, we consider a system under linearly polarized light along the x direction propagating along the y-z plane. We then replace the integration of k with $\varepsilon=\varepsilon^F_-$. We find that the real part of $\sigma_{xx}(q,\Omega)$ consists of four parts: $1/\Omega$, $2\mu^2\varepsilon/\sqrt{\varepsilon^2-\Delta_F^2}$, $e^2v_F^2\sin\theta^2\cos\phi^2$, and $\Delta_F^2(v_Fq\cdot\hat{k})^2/4\varepsilon^4$. Because $\sigma_{\alpha\alpha}(q,\Omega)=(i\hbar/\Omega)\,\mathrm{Im}\,K^R_{\alpha\alpha}(q,\Omega)$, the first three terms, like for normal optical conductivity, are due to the relation of the electron field and vector potential, the density of states, and the current coupling, respectively. The fourth term is specific to SWSMs. As we previously discussed, due to the opposite charges of quasiparticles in hole and electron states with the same chirality, the quasiparticle transition from a hole state to an electron state with the same $\mathbf{k}$ is forbidden. On the other hand, there is a finite overlap between the electron state with momentum $\mathbf{k}+\boldsymbol{q}$ and the hole state with momentum $\mathbf{k}$. The transition probability between these two states is found to be proportional to $\Delta_F^2(v_F\mathbf{q}\cdot\hat{\mathbf{k}})^2/4[\Delta_F^2+(v_Fk-\mu)]^2$. In addition, such a transition is forbidden if $\mathbf{q}$ is perpendicular to $\mathbf{k}$. Therefore, only the component of $\mathbf{q}$ parallel to $\mathbf{k}$ contributes to the optical conductivity. After using the dispersion relation for the photon, $\Omega=cq$, we finally find $\sigma^F_{xx}(q,\Omega)$:

$$\sigma^F_{xx}(\Omega)=\frac{2e^2\Delta_F^2\mu^2v_F}{15\pi\hbar^2c^2}\frac{\arctan\left(\frac{\sqrt{4\Delta_F^2-\Omega^2}}{\Omega}\right)+\frac{\pi}{2}}{\pi\Omega^2\sqrt{(\Omega/2)^2-\Delta_F^2}}.\quad(13)$$

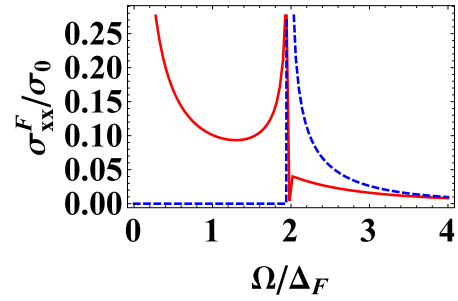

FIG. 2. The optical conductivity for SWSMs with the FFLO pairing. The dashed blue curve shows $\mathrm{Re}\,\sigma^F(\Omega)$, and the red solid curve shows $\mathrm{Im}\,\sigma^F(\Omega)$.

Figure 2 shows the optical conductivity in the FFLO case, $\sigma_{0,F/B}=e^2\mu^2v_F/4\pi\hbar^2c^2\Delta_{F/B}$. When $\Omega<2\Delta_F$, there is no available energy band for the electronic transition. As a result, $\mathrm{Re}\,\sigma^F(\Omega)=0$. $\mathrm{Im}\,\sigma^F(\Omega)$ is divergent at $\Omega=0$ and $\Omega=2\Delta_F$ because the densities of states at the edges of the conduction and valence bands are divergent. For $\Omega>2\Delta_F$, $\mathrm{Im}\,\sigma_F$ decreases from a finite value, while $\mathrm{Re}\,\sigma_F$ decays from infinity. The real part of the optical conductivity has a frequency threshold at $\Omega=2\Delta_F$. The singular response at the threshold in $\mathrm{Re}[\sigma^F_{xx}(q,\Omega)]$ provides a direct signature of the FFLO pairing.

We mentioned above that the conductivity in the clean limit does not involve any type of impurity scattering. In clean single-band superconductors, the combination of particle-hole and inversion symmetries prevents momentum-conserving transitions, and the conductivity vanishes. For SWSMs, there are multiple bands, and the bulk conductivity is nonzero in the clean limit; as a result, the optical transition is possible via direct band-to-band transition, and momentum relaxation is not required. The physical meaning of the optical conductivity in the clean limit is that it probes the interband transition, not the center of mass drifting. For graphene in the clean limit, the universal conductance is obtained by calculating the optical conductivity without any impurities [61,62].

(2) *BCS pairing.* Because of the anisotropy of the energy dispersion with the BCS pairing, the gap function goes to zero for certain directions imposed by symmetry. As a result, the optical conductivity exhibits anisotropic behavior and depends on the directions of light polarization and propagation ($\hat{k}_\alpha$ and $\widehat{\mathbf{q}}$). However, the energy spectrum shows a rotational invariance around k_z, and the optical conductivity depends on the orientation of the light. For light polarized in

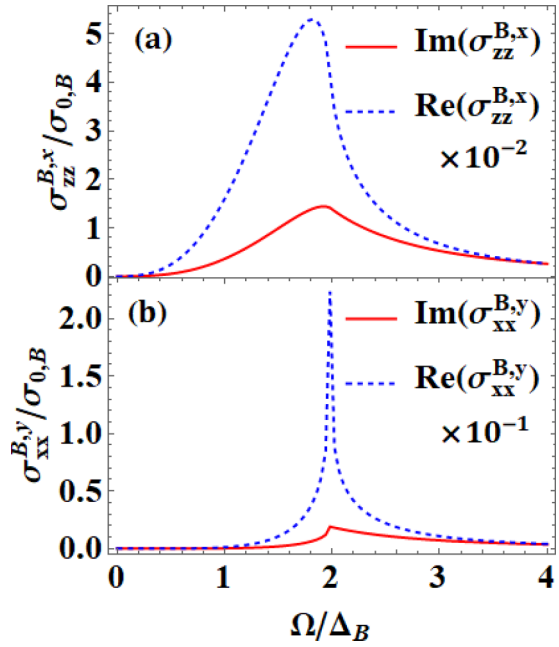

FIG. 3. The optical conductivity for SWSMs with the BCS pairing. (a) $\sigma_{zz}^{B,x}$ and (b) $\sigma_{xx}^{B,y}$. The red solid curves show the real parts of the optical conductivities, and the blue dashed curves show the imaginary parts of the optical conductivities.

the direction $\hat{k}_\alpha$ and propagating in the direction $\hat{q}$, the optical conductivity has the same form as Eq. (12), $\sigma_{\alpha\alpha}^{B,\hat{\mathbf{q}}}(q,\Omega) = (2\pi\hbar)^{-3}\int d^3k g(k)(\mathbf{q}\cdot\hat{\mathbf{k}})^2\hat{k}_\alpha^2$, if we replace Δ^F with $\Delta_B\sin\theta$ and replace $\varepsilon_-^F(k)$ by $\varepsilon_-^B(k)$. Here $\theta = \cos^{-1}k_z/k$, and $\varepsilon_-^B(k) = \sqrt{\Delta_B^2 + v_F^2k^2 + \mu^2 - 2v_F\sqrt{\Delta_B^2k_z^2 + k^2\mu^2}}$. Like in the analysis of FFLO pairing, the real part also consists of four contributions. By defining $\boldsymbol{q} = q(\sin\theta'\cos\phi', \sin\theta'\sin\phi', \cos\theta')$ and $\hat{\mathbf{k}} = (\sin\theta\cos\phi, \sin\theta\sin\phi, \cos\theta)$, the relation $\sigma_{zz}^{B,x}(q,\Omega) = \sigma_{xx}^{B,z}(q,\Omega)$ can be confirmed. This is the exchange symmetry for the orientations of q and α in optical conductivity. $\sigma_{\alpha\alpha}^{B,\hat{q}}(q,\Omega)$ can be expressed in the form $\sigma_{\alpha\alpha}^{B,\hat{\mathbf{q}}}(\Omega) = (2\pi\hbar)^{-3}\int d^3k g(k)(\mathbf{q}\cdot\hat{\mathbf{k}})^2(\hat{\mathbf{e}}_\alpha\cdot\hat{\mathbf{k}})^2$, where $\hat{\mathbf{e}}_\alpha$ is the unit vector of the direction α. By using the photon dispersion relation, $\Omega = cq$, we finally find $\sigma_{zz}^{B,\hat{\mathbf{q}}}(\Omega)$ and $\sigma_{xx}^{B,\hat{\mathbf{q}}}(\Omega)$:

$$\sigma_{zz(xx)}^{B,\hat{\mathbf{q}}}(q,\Omega) = \frac{v_F e^2\Delta_B^2\mu^2}{(\pi\hbar)^2c^2}\int_0^{\arcsin\frac{\Omega}{2\Delta_B}} d\theta\,\Lambda_{zz(xx)}(\theta,\theta') \times \frac{\frac{\pi}{2} - i\,\mathrm{arctanh}\left(\frac{\sqrt{\Omega^2-4\Delta_B^2\sin\theta^2}}{\Omega}\right)}{\Omega^2\sqrt{\Omega^2-4\Delta_B^2\sin\theta^2}}, \quad (14)$$

where $\Lambda_{zz}(\theta,\theta') = \cos^2\theta\sin^5\theta$ and $\Lambda_{xx}(\theta,\theta') = \sin^7\theta\sin^2\theta'/4 + \cos^2\theta\sin^5\theta\cos^2\theta'$.

We show the conductivities of two special cases, $\sigma_{zz}^{B,\hat{\mathbf{e}}_x}(\Omega)$ and $\sigma_{xx}^{B,\hat{\mathbf{e}}_y}(\Omega)$, in Fig. 3. The general case $\sigma_{xx}^{B,\hat{\mathbf{q}}}(\Omega)|_{\hat{\mathbf{q}}=(0,\sin\theta',\cos\theta')}$ can be obtained with the combination $\sigma_{xx}^{B,\hat{\mathbf{q}}}(\Omega)|_{\hat{\mathbf{q}}=(0,\sin\theta',\cos\theta')} = \sin^2\theta'\sigma_{xx}^{B,\hat{\mathbf{e}}_y}(\Omega) + \cos^2\theta'\sigma_{zz}^{B,\hat{\mathbf{e}}_x}(\Omega)$ for $\hat{\mathbf{q}} = (0,\sin\theta',\cos\theta')$. Figure 3(a) shows the optical conductivity $\sigma_{zz}^{B,\hat{x}}(\Omega)$. The light is polarized along the z direction, and the transport direction is x. Figure 3(b) shows the optical conductivity $\sigma_{xx}^{B,\hat{y}}(\Omega)$. The light is polarized along the x direction, and the transport direction is y. When $\Omega < 2\Delta_B$, the real and imaginary parts of the optical conductivity, $\sigma_{xx}^{B,\hat{y}}$ and $\sigma_{zz}^{B,\hat{x}}(\Omega)$, start from zero and follow power law behaviors $\propto\Omega^5$ and $\propto\Omega^3$, respectively. Both reach peak values at Ω slightly below $2\Delta_B$. $\sigma_{xx}^{B,\hat{y}}$ is sharply peaked around $2\Delta_B$. Around $\Omega = 2\Delta_B$, both $\mathrm{Re}\,\sigma_{xx}^{B,\hat{y}}$ and $\mathrm{Re}\,\sigma_{zz}^{B,\hat{x}}(\Omega)$ give rise to a maximum response, as observed in the experiment. In particular, the Van Hove resonance in $\mathrm{Re}\,\sigma_{xx}^{B,\hat{y}}$ provides a direct signature of the BCS pairing in SWSMs. The quite different frequency characteristics of $\mathrm{Re}\,\sigma_{xx}^{B,\hat{y}}$ and $\mathrm{Re}\,\sigma_{zz}^{B,\hat{x}}(\Omega)$ are closely related to the optical transition rate governed by the band dispersion along the x and z directions. The peaks near $2\Delta_B$ for $\mathrm{Re}\,\sigma_{zz}^{B,\hat{x}}(\Omega)$ and at $2\Delta_B$ for $\mathrm{Re}\,\sigma_{xx}^{B,\hat{y}}$ are due to the resonant transition between the bottom of the lower band and the top of the upper band. Along the x direction, the dispersion is flat for both the lower and upper bands, which leads to a resonant transition. As a result, $\mathrm{Re}\,\sigma_{xx}^{B,\hat{y}}$ is sharply peaked at $2\Delta_B$. Along the z direction, the bands are more dispersive, although they can also be viewed as flat at one point (highest and lowest). The more dispersive bands result in a much broader peak whose height is also lower.

Different from the clean limit where the energy and momentum are conserved, there are many cases in which the momentum conservation could be broken due to the reflection of electrons by the interface and the scattering of electrons by impurities near the interface, such as in dirty superconductors and thin films. The carrier mean free path or film thickness d is much smaller than the coherence length. The optical conductivity in superconductors without momentum conservation can be calculated using the Mattis-Bardeen formula [52]. Despite the presence of gapless Weyl points, the bulk response is reminiscent of the Mattis-Bardeen result for s-wave superconductors, as the order parameter can be averaged to zero by sufficiently strong scattering around the Fermi surface. The conductivity is related to the surface electrodynamic properties of the superconductor such as the surface impedance, penetration depth, and anomalous skin effect. By assuming the Mattis-Bardeen theory is applicable to SWSMs, we calculate the optical conductivity in SWSMs in the dirty limit. At zero temperature, the optical conductivity can be written as

$$\sigma_{\alpha\beta} = \frac{e^2}{\hbar\Omega}\sum_{\mathbf{k}} v_\alpha v_\beta\left[\left(1-\frac{\xi_+}{E_+}\right)\left(1+\frac{\xi_-}{E_-}\right) - \frac{\Delta_+\Delta_-}{E_+E_-}\right] \times \frac{1}{\hbar\Omega - E_+ - E_- + i0^+}, \quad (15)$$

where $E_\pm = \sqrt{(v_Fk_\pm - \mu)^2 + \Delta_\pm^2}$, $\xi_\pm = v_Fk_\pm - \mu$, $k_\pm = k \pm q/2$, and $\Delta_\pm$ is the energy gap corresponding to momenta $k_\pm$. Since $qv_F \gg \Delta$, we use Abrikosov's replacement $\sum_{\mathbf{k}} \to [N(0)/(4qv_F)]\int d\xi_+ d\xi_-$ [63].

For the FFLO pairing in dirty SWSMs and thin films, the superconducting energy gap is isotropic, and the

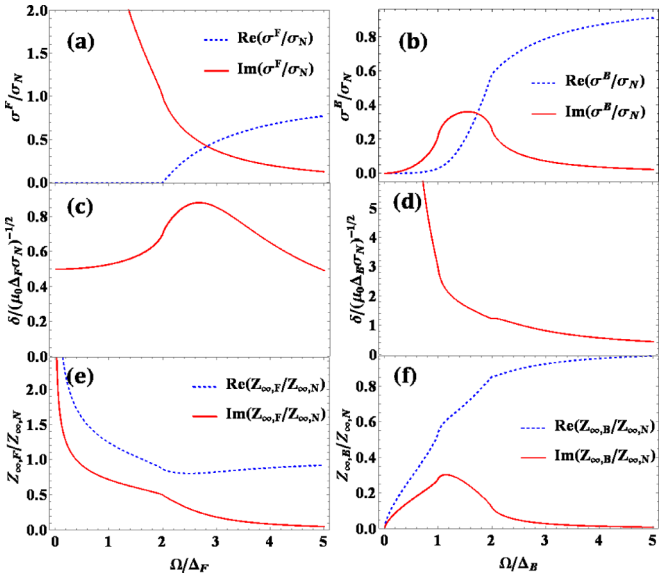

FIG. 4. FFLO and BCS cases in the dirty limit. (a) and (b) Optical conductivity; the dashed blue curve shows $\mathrm{Re}\,\sigma(\Omega)$, and the red curve shows $\mathrm{Im}\,\sigma(\Omega)$. (c) and (d) Penetration depth l. (e) and (f) Surface impedance $Z_{\infty,S}/Z_{\infty,N}$. (a), (c), and (e) are for the FFLO case, while (b), (d), and (f) are for the BCS case.

Mattis-Bardeen equation at zero temperature [64,65] can be simplified to

$$\frac{\sigma^F(\Omega,0)}{\sigma_N} = -\frac{1}{\Omega}\int_{\Delta_F-\hbar\Omega}^{\Delta_F} dE\,\frac{E^2+\Delta_F^2+\hbar\Omega E}{D^F(E,0)D^F(E,\Omega)}, \tag{16}$$

where σ_N is the real part of the conductivity of the normal state and $D^F(E,\Omega)=\sqrt{(\hbar\Omega+E)^2-\Delta_F^2}$. Since we are interested in only the regime near the Fermi surface, $\Omega\approx\Delta_F$, $k_\pm=\mu/v_F$, and v_α^2 replaces $v_F^2/3$ in the integration.

Because the gap is anisotropic for the SWSM with BCS pairing, we expand the general Mattis-Bardeen equation to anisotropic cases. $E_\pm=\sqrt{v_F^2k_\pm^2-\sqrt{\mu^2+\Delta_B^2\cos^2\theta_\pm}}$ is angle dependent, where $\theta_\pm$ are the angles between $\mathbf{k}_\pm$ and $\mathbf{k}$. The angle-dependent extension of the Mattis-Bardeen equation [54] at zero temperature is given by

$$\begin{aligned}\frac{\sigma^B(\Omega,0)}{\sigma_N} &= -\frac{1}{\Omega}\int_{-\hbar\Omega}^{0} dE\left\langle\frac{E}{D^B(E,0,\theta)}\right\rangle_\theta\left\langle\mathrm{Re}\,\frac{\hbar\Omega+E}{D^B(E,\Omega,\theta')}\right\rangle_{\theta'}\\ &\quad-\frac{1}{\Omega}\int_{-\hbar\Omega}^{0} dE\left\langle\frac{\Delta_B\sin\theta}{D^B(E,0,\theta)}\right\rangle_\theta\left\langle\mathrm{Re}\,\frac{\Delta_B\sin\theta'}{D^B(E,\Omega,\theta')}\right\rangle_{\theta'},\end{aligned} \tag{17}$$

where $\langle f(\theta)\rangle_\theta=(1/\pi)\int_0^\pi d\theta\sin\theta f(\theta)$ and $D^B(\varepsilon,\Omega,\theta)=\sqrt{(\hbar\Omega+\varepsilon)^2-\Delta_B^2\sin^2\theta}$.

The optical properties in the dirty limit are shown in Fig. 4. Figure 4(a) shows the optical conductivity for FFLO pairing, where the red solid curve shows $\mathrm{Im}\,\sigma^F(\Omega)$ and the blue dashed curve shows $\mathrm{Re}\,\sigma^F(\Omega)$. If the photon energy is lower than $2\Delta_F$, $\mathrm{Re}\,\sigma^F(\Omega)$ vanishes. Starting from $2\Delta_F$, it increases gradually to nearly 1 due to the quasiparticle excitations across the energy gap. This is significantly different from that in the clean limit. The imaginary part of optical conductivity is proportional to Ω^{-1} for $\Omega<2\Delta_F$ and changes to a power law behavior $\propto\Omega^{-2}$ for $\Omega>2\Delta_F$. Such behavior agrees with many experimental results for s-wave superconductors [23,24]. The optical conductivity for BCS pairing is shown in Fig. 4(b). Both the real and imaginary parts of the optical conductivity are zero at $\Omega=0$. The real part increases with a power law behavior of Ω^4 for $\Omega<2\Delta_B$, then saturates to 1 for $\Omega>2\Delta_F$. The imaginary part of the optical conductivity is proportional to Ω^2 for $\Omega<\Delta_B$. After reaching a maximum for $\Delta_B<\Omega<2\Delta_B$, it drops to zero for $\Omega>2\Delta_B$.

The surface optical conductivity is related to other physical quantities of superconductors, for example, the penetration depths $l(\Omega)$ and the surface impedances. The penetration depth is related to the optical conductivity as $l(\Omega)=\{\Omega\mu_0[|\sigma(\Omega)|+\mathrm{Im}\sigma(\Omega)]/2\}^{-1/2}$, where μ_0 is the vacuum permeability. The surface impedance in the extreme anomalous limit can be used to interpret the anomalous skin effect through the function of surface optical conductivity [52]. The impedance is given as $Z_{\infty,S}/Z_{\infty,N}=\sqrt[3]{\{\mathrm{Re}[\sigma_S(\Omega)]-i\,\mathrm{Im}[\sigma_S(\Omega)]\}/\sigma_N}$, where $Z_{\infty,S/N}$ is the surface impedance of superconducting/normal states. In Figs. 4(c) and 4(d), we show the penetration depth as a function of frequency. It is found that due to a large phase difference between the field and carriers under BCS pairing (or the delayed carrier response), the field can penetrate much deeper than in the case of FFLO pairing. As frequency increases, more scattering phase space opens up, the response delay decreases, and the penetration decreases. A similar analysis applies to the FFLO case. Figures 4(e) and 4(f) show the surface impedance as a function of frequency. Both the real and imaginary parts of the surface impedance for FFLO pairing decrease as Ω increases. The trend of surface impedance for BCS pairing is similar to the surface optical conductivity.

IV. DISCUSSION AND CONCLUSION

We obtained the frequency-dependent conductivity of SWSMs with FFLO and BCS pairing. Different pairings result in distinct frequency characteristics of the optical conductivity in both the clean and dirty limits. The calculated conductivity can be used to derive other useful physical quantities. For example, by comparing the calculated conductivity to the Drude formula for conductivity, $\sigma(\Omega)=i\omega_p^2/[4\pi\lambda(\Omega+i\tau^{-1})]$, we can deduce the effect of relaxation, where ω_p^2 is the oscillator strength, λ is the mass enhancement factor, and τ^{-1} is the scattering rate, with $\lambda(\Omega)=(\omega_p^2/4\pi\Omega)\,\mathrm{Im}[1/\sigma(\Omega)]$ and $1/\tau(\Omega)=-(\omega_p^2/4\pi\hbar)\,\mathrm{Re}[1/\sigma(\Omega)]$. In the following, we discuss some other points related to our model and results.

The node in the band dispersion is not unique in SWSMs. The result presented here should be distinguished from that in a regular superconductor with nodes. In a topologically trivial one-band superconductor, the dissipative part of the bulk optical conductivity vanishes in the clean limit. This is due to the orthogonality of positive- and negative-energy bulk states and the lack of a matrix structure for the current operator, despite the particle-hole hybridization induced by pairing.

In contrast to regular superconductors, the Fermi surface breaks up into disconnected sheets which enclose one Weyl node. The unusual band structure of SWSMs around the Weyl point results in different contributions to the current response. Specifically, it can be seen from the flow correlation in conductivity calculations. The operator $\sigma_{\alpha,\kappa} = (1 - 2\delta_{\kappa,-1}\delta_{\alpha,z})\sigma_\alpha$ in the current operator in Eq. (8) reflects the difference from conventional current operators. Correspondingly, the response kernel $K_{\alpha\gamma}(q, i\Omega)$ takes the form

$$\begin{aligned} &K_{\alpha\gamma}(q, i\Omega) \\ &= -\frac{(ev_F)^2}{V}\sum_{\kappa,\kappa'}\iint\frac{dkdk'}{(2\pi\hbar)^6}\int_0^{\hbar\beta} d\tau e^{i\Omega\tau/\hbar} \\ &\quad\times\{\delta(k'-hk-q)\delta_{\kappa,\kappa'}\mathrm{Tr}[G_\kappa(k+q,-\tau) \\ &\quad\times\sigma_{\alpha,\kappa}G_\kappa(k,\tau)\sigma^*_{\gamma,\kappa}] - \delta(k'+k)\delta_{\kappa,\lambda\kappa'}\mathrm{Tr} \\ &\quad\times\left[F^{\dagger T}_{\lambda,\kappa}(k'-q,-\tau)\sigma_x\sigma_{\alpha,\kappa}\sigma_x F_{\lambda,\kappa}(-k,\tau)\sigma^*_{\gamma,\lambda\kappa}\right]\}, \quad (18) \end{aligned}$$

where $\lambda = \pm 1$ for the FFLO pairing and the BCS pairing, respectively, and the Green's function $G_\kappa(\mathbf{k}, \tau)$ and the correlation functions $F_{\lambda,\kappa}(\mathbf{k}, \tau)$ are node dependent.

It is not straightforward to measure what type of potential is responsible for the superconducting pairing. The optical conductivity is not the only way to distinguish the pairing potentials. Since the pairing potential correlates the density of states, one can also measure other quantities (electronic or magnetic) that are closely correlated to the density of states to identify pairing in SWSMs. In terms of sensitivity, the optical conductivity measured through transmission (or reflection) spectroscopy usually has an uncertainly of less than 10%. This sensitivity should enable a distinction of the two types of conductivity resonances.

SWSM materials may have multiband structures and can be described by more than one order parameter. There also could be order parameters with different symmetries in one material. The nature of the pairing counterparts (s wave or p wave) in SWSMs has not been unambiguously determined either. Some studies suggest that the p-wave states are thermodynamically indistinguishable from s-wave states and the parallel-spin triplet states are much more resilient to externally applied magnetic field. Probes for p-wave superconductivity have not been settled. Our result does not address whether the s-wave phase or p-wave phase dominates, which is a separate topic to be studied theoretically and experimentally. The problem we solved is limited to the s-wave pairing state, and our conclusion does not extend to systems with other symmetries.

Finally, we would like to mention some possible SWSM candidates for measuring the optical conductivity. Recently, superconductivity was studied in several Weyl semimetal materials such as $MoTe_2$, which exhibits superconductivity with a transition temperature of 0.10 K [1]. The superconductivity arising from a Weyl semimetal normal phase in $MoTe_{1.85}Se_{0.15}$ makes it a promising candidate for realizing topological superconductivity [66]. Experimentally, superconductivity has been reported in the B phase of UPt_3 [67], SrPtAs [68], and praseodymium-based compounds (e.g., $PrOs_4Sb_{12}$ and $PrPt_4Ge_{12}$ [69]). These systems in which superconductivity has been detected are possible candidates for optical measurement.

In summary, the optical response of SWSMs provides valuable information about the symmetry of the superconducting energy gap for FFLO and BCS pairings. The photon response process includes contributions from the quasiparticle, photon, and Cooper pair. We showed that the resonance at the threshold and the Von Hove resonance in the optical conductivity are distinct signatures of FFLO and BCS pairings in SWSMs. Based on the exhibited characteristics of different light absorption behaviors, we suggest using optical means to distinguish which superconductivity pairing dominates in a SWSM. Finally, while the optical response reveals the superconducting pairing potential, the microscopic mechanism determining which pairing is favored in a system cannot be obtained from the optical conductivity.

ACKNOWLEDGMENTS

The authors are thankful for the support of the NSFC (Grants No. 11274013 and No. 11774006), NBRP of China (Grant No. 2012CB921300), and the Australian Research Council (Grant No. DP230102221).

[1] Y. Qi *et al.*, Nat. Commun. **7**, 11038 (2016).
[2] S. A. Yang, H. Pan, and F. Zhang, Phys. Rev. Lett. **113**, 046401 (2014).
[3] G. Bednik, A. A. Zyuzin, and A. A. Burkov, Phys. Rev. B **92**, 035153 (2015).
[4] T. Zhou, Y. Gao, and Z. D. Wang, Phys. Rev. B **93**, 094517 (2016).
[5] Y. Li and F. D. M. Haldane, Phys. Rev. Lett. **120**, 067003 (2018).
[6] B. Lu, K. Yada, M. Sato, and Y. Tanaka, Phys. Rev. Lett. **114**, 096804 (2015).
[7] P. Hosur, X. Dai, Z. Fang, and X.-L. Qi, Phys. Rev. B **90**, 045130 (2014).
[8] M. Alidoust, K. Halterman, and A. A. Zyuzin, Phys. Rev. B **95**, 155124 (2017).
[9] T. Meng and L. Balents, Phys. Rev. B **86**, 054504 (2012).
[10] G. Y. Cho, J. H. Bardarson, Y.-M. Lu, and J. E. Moore, Phys. Rev. B **86**, 214514 (2012).
[11] P. Fulde and R. A. Ferrell, Phys. Rev. **135**, A550 (1964).
[12] A. Larkin and Y. N. Ovchinnikov, Sov. Phys. JETP **20**, 762 (1965).
[13] J. Fang, C. Zhang, and Z. S. Ma, Phys. Rev. B **107**, 144512 (2023).
[14] W. Chen, L. Jiang, R. Shen, L. Sheng, B. Wang, and D. Xing, Europhys. Lett. **103**, 27006 (2013).

[15] J. Fang, W. Duan, J. Liu, C. Zhang, and Z. S. Ma, Phys. Rev. B **97**, 165301 (2018).

[16] W. Y. Duan, J. F. Liu, J. Fang, C. Zhang, and Z. S. Ma, Phys. Rev. B **98**, 155317 (2018).

[17] K. A. Madsen, E. J. Bergholtz, and P. W. Brouwer, Phys. Rev. B **95**, 064511 (2017).

[18] J. Xiao, Y. Vituri, and E. Berg, Phys. Rev. B **108**, 094520 (2023).

[19] G. Li, W. Z. Hu, J. Dong, Z. Li, P. Zheng, G. F. Chen, J. L. Luo, and N. L. Wang, Phys. Rev. Lett. **101**, 107004 (2008).

[20] P. Samuely, P. Szabó, Z. Pribulová, M. E. Tillman, S. L. Bud'ko, and P. C. Canfield, Supercond. Sci. Technol. **22**, 014003 (2009).

[21] H. Chen, Phys. Rev. Lett. **71**, 2304 (1993).

[22] A. Charnukha, D. Pröpper, N. D. Zhigadlo, M. Naito, M. Schmidt, Z. Wang, J. Deisenhofer, A. Loidl, B. Keimer, A. V. Boris, and D. N. Basov, Phys. Rev. Lett. **120**, 087001 (2018).

[23] M. Thiemann, M. H. Beutel, M. Dressel, N. R. Lee-Hone, D. M. Broun, E. Fillis-Tsirakis, H. Boschker, J. Mannhart, and M. Scheffler, Phys. Rev. Lett. **120**, 237002 (2018).

[24] M. Thiemann, M. Dressel, and M. Scheffler, Phys. Rev. B **97**, 214516 (2018).

[25] T. Cea, D. Bucheli, G. Seibold, L. Benfatto, J. Lorenzana, and C. Castellani, Phys. Rev. B **89**, 174506 (2014).

[26] E. Schachinger and J. P. Carbotte, Phys. Rev. B **95**, 144516 (2017).

[27] S. V. Dordevic, D. van der Marel, and C. C. Homes, Phys. Rev. B **90**, 174508 (2014).

[28] T. Mori, E. J. Nicol, S. Shiizuka, K. Kuniyasu, T. Nojima, N. Toyota, and J. P. Carbotte, Phys. Rev. B **77**, 174515 (2008).

[29] Z. Tagay, F. Mahmood, A. Legros, T. Sarkar, R. L. Greene, and N. P. Armitage, Phys. Rev. B **104**, 064501 (2021).

[30] E. J. Singley, D. N. Basov, E. D. Bauer, and M. B. Maple, Phys. Rev. B **65**, 161101(R) (2002).

[31] R. Cervasio, L. Tomarchio, M. Verseils, J.-B. Brubach, S. Macis, S. Zeng, A. Ariando, P. Roy, and S. Lupi, ACS Appl. Electron. Mater. **5**, 4770 (2023).

[32] L. Benfatto, C. Castellani, and G. Seibold, Phys. Rev. B **108**, 134508 (2023).

[33] H. Suzuki, M. Minola, Y. Lu, Y. Peng, R. Fumagalli, E. Lefrançois, T Loew, J. Porras, K. Kummer, D. Betto, S. Ishida, H. Eisaki, C. Hu, X. Zhou, M. W. Haverkort, N. B. Brookes, L. Braicovich, G. Ghiringhelli, M. L. Tacon, and B. Keimer, npj Quantum Mater. **3**, 65 (2018).

[34] N. R. Lee-Hone, V. Mishra, D. M. Broun, and P. J. Hirschfeld, Phys. Rev. B **98**, 054506 (2018).

[35] G. Kim, K. S. Rabinovich, A. V. Boris, A. N. Yaresko, Y. E. Suyolcu, Y.-M. Wu, P. A. van Aken, G. Christiani, G. Logvenov, and B. Keimer, Proc. Natl. Acad. Sci. USA **118**, e2106170118 (2021).

[36] A. Charnukha, J. Phys.: Condens. Matter **26**, 253203 (2014).

[37] C. Mirri, P. Calvani, F. M. Vitucci, A. Perucchi, K. W. Yeh, M. K. Wu, and S. Lupi, Supercond. Sci. Technol. **25**, 045002 (2012).

[38] A. Charnukha, J. Deisenhofer, D. Pröpper, M. Schmidt, Z. Wang, Y. Goncharov, A. N. Yaresko, V. Tsurkan, B. Keimer, A. Loidl, and A. V. Boris, Phys. Rev. B **85**, 100504(R) (2012).

[39] C. C. Homes, Z. J. Xu, J. S. Wen, and G. D. Gu, Phys. Rev. B **85**, 180510(R) (2012).

[40] C. C. Homes, Y. M. Dai, J. S. Wen, Z. J. Xu, and G. D. Gu, Phys. Rev. B **91**, 144503 (2015).

[41] R. P. S. M. Lobo, G. Chanda, A. V. Pronin, J. Wosnitza, S. Kasahara, T. Shibauchi, and Y. Matsuda, Phys. Rev. B **91**, 174509 (2015).

[42] B. Xu, Z. C. Wang, E. Sheveleva, F. Lyzwa, P. Marsik, G. H. Cao, and C. Bernhard, Phys. Rev. B **99**, 125119 (2019).

[43] R. Yang, J. W. Huang, N. Zaki, I. Pletikosić, Y. M. Dai, H. Xiao, T. Valla, P. D. Johnson, X. J. Zhou, X. G. Qiu, and C. C. Homes, Phys. Rev. B **100**, 235132 (2019).

[44] E. Uykur, B. R. Ortiz, O. Iakutkina, M. Wenzel, S. D. Wilson, M. Dressel, and A. A. Tsirlin, Phys. Rev. B **104**, 045130 (2021).

[45] J. Ahn and N. Nagaosa, Nat. Commun. **12**, 1617 (2021).

[46] T. Xu, T. Morimoto, and J. E. Moore, Phys. Rev. B **100**, 220501(R) (2019).

[47] K. Takasan, T. Morimoto, J. Orenstein, and J. E. Moore, Phys. Rev. B **104**, L161202 (2021).

[48] T. Yu, J. Wright, G. Khalsa, B. Pamuk, C. S. Chang, Y. Matveyev, X. Wang, T. Schmitt, D. Feng, D. A. Muller, H. G. Xing, D. Jena, and V. N. Strocov, Sci. Adv. **7**, eabi5833 (2021).

[49] C. C. Homes, J. J. Tu, J. Li, G. D. Gu, and A. Akrap, Sci. Rep. **3**, 3446 (2013).

[50] Y. Murotani and R. Shimano, Phys. Rev. B **99**, 224510 (2019).

[51] M. J. Calderón and E. Bascones, npj Quantum Mater. **5**, 57 (2020).

[52] D. Mattis and J. Bardeen, Phys. Rev. **111**, 412 (1958).

[53] G. Seibold, L. Benfatto, and C. Castellani, Phys. Rev. B **96**, 144507 (2017).

[54] M. Papaj and J. E. Moore, Phys. Rev. B **106**, L220504 (2022).

[55] S. Ono and K. Shiozaki, Phys. Rev. X **12**, 011021 (2022).

[56] P. J. D. Crowley and L. Fu, Phys. Rev. B **106**, 214526 (2022).

[57] T. C. Wu, H. K. Pal, and M. S. Foster, Phys. Rev. B **103**, 104517 (2021).

[58] G. D. Mahan, *Many-Particle Physics* (Kluwer Academic/Plenum Publishers, New York, 2000).

[59] D. Y. Vodolazov, Phys. Rev. Appl. **7**, 034014 (2017).

[60] Q. Wang, H.-Y. Chen, C.-R. Hu, and C. S. Ting, Phys. Rev. Lett. **96**, 117006 (2006)

[61] T. Stauber, N. M. R. Peres, and A. K. Geim, Phys. Rev. B **78**, 085432 (2008).

[62] R. R. Nair, P. Blake, A. N. Grigorenko, K. S. Novoselov, T. J. Booth, T. Stauber, N. M. R. Peres, and A. K. Geim, Science **320**, 1308 (2008)

[63] A. A. Abrikosov, *Fundamentals of the Theory of Metals* (North-Holland, Amsterdam, 1988).

[64] T. Yanagisawa, S. Koikegami, H. Shibata, S. Kimura, S. Kashiwaya, A. Sawa, N. Matsubara, and K. Takita, J. Phys. Soc. Jpn. **70**, 2833 (2001).

[65] P. Hirschfeld, W. Putikka, P. Wölfle, and Y. Campbell, J. Low. Temp. Phys. **88**, 395 (1992).

[66] Z. Wang, J. Olivares, H. Namiki, V. Pareek, K. Dani, T. Sasagawa, V. Madhavan, and Y. Okada, Phys. Rev. B **104**, 115102 (2021).

[67] Y. Yanase, Phys. Rev. B **94**, 174502 (2016).

[68] M. H. Fischer, T. Neupert, C. Platt, A. P. Schnyder, W. Hanke, J. Goryo, R. Thomale, and M. Sigrist, Phys. Rev. B **89**, 020509(R) (2014).

[69] V. Kozii, J. W. F. Venderbos, and L. Fu, Sci. Adv. **2**, e1601835 (2016).